Nuclear Instruments and Methods in Physics Research A 618 (2010) 139–152

Contents lists available at ScienceDirect

Nuclear Instruments and Methods in Physics Research A

journal homepage: www.elsevier.com/locate/nima

Calibration and characterization of the IceCube photomultiplier tube

R. Abbasi [z], Y. Abdou [t], T. Abu-Zayyad [af], J. Adams [o], J.A. Aguilar [z], M. Ahlers [ae], K. Andeen [z], J. Auffenberg [al], X. Bai [ad], M. Baker [z], S.W. Barwick [v], R. Bay [g], J.L. Bazo Alba [am], K. Beattie [h], J.J. Beatty [q,r], S. Bechet [l], J.K. Becker [j], K.-H. Becker [al], M.L. Benabderrahmane [am], J. Berdermann [am], P. Berghaus [z], D. Berley [p], E. Bernardini [am], D. Bertrand [l], D.Z. Besson [x], M. Bissok [a], E. Blaufuss [p], D.J. Boersma [a], C. Bohm [ag], O. Botner [aj], L. Bradley [ai], J. Braun [z], S. Buitink [h], M. Carson [t], D. Chirkin [z], B. Christy [p], J. Clem [ad], S. Cohen [w], C. Colnard [u], D.F. Cowen [ai,ah], M.V. D'Agostino [g], M. Danninger [ag], C. De Clercq [m], L. Demirörs [w], O. Depaepe [m], F. Descamps [t], P. Desiati [z], G. de Vries-Uiterweerd [t], T. DeYoung [ai], J.C. Díaz-Vélez [z], J. Dreyer [s,j], J.P. Dumm [z], M.R. Duvoort [ak], R. Ehrlich [p], J. Eisch [z], R.W. Ellsworth [p], O. Engdegård [aj], S. Euler [a], P.A. Evenson [ad], O. Fadiran [d], A.R. Fazely [f], T. Feusels [t], K. Filimonov [g], C. Finley [ag], M.M. Foerster [ai], B.D. Fox [ai], A. Franckowiak [i], R. Franke [am], T.K. Gaisser [ad], J. Gallagher [y], R. Ganugapati [z], M. Geisler [a], L. Gerhardt [h,g], L. Gladstone [z], A. Goldschmidt [h], J.A. Goodman [p], D. Grant [ai], T. Griesel [ab], A. Groß [o,u], S. Grullon [z], R.M. Gunasingha [f], M. Gurtner [al], C. Ha [ai], A. Hallgren [aj], F. Halzen [z], K. Han [o], K. Hanson [z], Y. Hasegawa [n], J. Haugen [z], K. Helbing [al], P. Herquet [ac], S. Hickford [o], G.C. Hill [z], K.D. Hoffman [p], A. Homeier [i], K. Hoshina [z], D. Hubert [m], W. Huelsnitz [p], J.-P. Hülß [a], P.O. Hulth [ag], K. Hultqvist [ag], S. Hussain [ad], R.L. Imlay [f], M. Inaba [n], A. Ishihara [n], J. Jacobsen [z], G.S. Japaridze [d], H. Johansson [ag], J.M. Joseph [h], K.-H. Kampert [al], A. Kappes [z,1], T. Karg [al], A. Karle [z], J.L. Kelley [z], N. Kemming [i], P. Kenny [x], J. Kiryluk [h,g], F. Kislat [am], N. Kitamura [z], S.R. Klein [h,g], S. Knops [a], G. Kohnen [ac], H. Kolanoski [i], L. Köpke [ab], D.J. Koskinen [ai], M. Kowalski [k], T. Kowarik [ab], M. Krasberg [z], T. Krings [a], G. Kroll [ab], K. Kuehn [q], T. Kuwabara [ad], M. Labare [l], S. Lafebre [ai], K. Laihem [a], H. Landsman [z], R. Lauer [am], A. Laundrie [z], R. Lehmann [i], D. Lennarz [a], J. Lünemann [ab], J. Madsen [af], P. Majumdar [am], R. Maruyama [z], K. Mase [n,*], H.S. Matis [h], M. Matusik [al], K. Meagher [p], M. Merck [z], P. Mészáros [ah,ai], T. Meures [a], E. Middell [am], N. Milke [s], H. Miyamoto [n], T. Montaruli [z,2], R. Morse [z], S.M. Movit [ah], R. Nahnhauer [am], J.W. Nam [v], U. Naumann [al], P. Nießen [ad], D.R. Nygren [h], S. Odrowski [u], A. Olivas [p], M. Olivo [aj,j], M. Ono [n], S. Panknin [i], L. Paul [a], C. Pérez de los Heros [aj], J. Petrovic [l], A. Piegsa [ab], D. Pieloth [s], A.C. Pohl [aj,3], R. Porrata [g], J. Posselt [al], P.B. Price [g], M. Prikockis [ai], G.T. Przybylski [h], K. Rawlins [c], P. Redl [p], E. Resconi [u], W. Rhode [s], M. Ribordy [w], A. Rizzo [m], P. Robl [aa], J.P. Rodrigues [z], P. Roth [p], F. Rothmaier [ab], C. Rott [q], C. Roucelle [u], D. Rutledge [ai], B. Ruzybayev [ad], D. Ryckbosch [t], H.-G. Sander [ab], P. Sandstrom [z], S. Sarkar [ae], K. Schatto [ab], S. Schlenstedt [am], T. Schmidt [p], D. Schneider [z], A. Schukraft [a], A. Schultes [al], O. Schulz [u], M. Schunck [a], D. Seckel [ad], B. Semburg [al], S.H. Seo [ag], Y. Sestayo [u], S. Seunarine [o], A. Silvestri [v], A. Slipak [ai], G.M. Spiczak [af], C. Spiering [am], M. Stamatikos [q,4], T. Stanev [ad], G. Stephens [ai], T. Stezelberger [h], R.G. Stokstad [h], S. Stoyanov [ad], E.A. Strahler [m], T. Straszheim [p], G.W. Sullivan [p], Q. Swillens [l], I. Taboada [e], A. Tamburro [af], O. Tarasova [am], A. Tepe [e], S. Ter-Antonyan [f], C. Terranova [w], S. Tilav [ad], P.A. Toale [ai], D. Tosi [am], D. Turčan [p], N. van Eijndhoven [m], J. Vandenbroucke [g], A. Van Overloop [t], J. van Santen [i], B. Voigt [am], D. Wahl [aa], C. Walck [ag], T. Waldenmaier [i], M. Wallraff [a], M. Walter [am], C. Wendt [z,*], S. Westerhoff [z], N. Whitehorn [z], K. Wiebe [ab], C.H. Wiebusch [a], G. Wikström [ag], D.R. Williams [b], R. Wischnewski [am], H. Wissing [p], K. Woschnagg [g], C. Xu [ad], X.W. Xu [f], G. Yodh [v], S. Yoshida [n,*], P. Zarzhitsky [b]

[a] III. Physikalisches Institut, RWTH Aachen University, D-52056 Aachen, Germany
[b] Department of Physics and Astronomy, University of Alabama, Tuscaloosa, AL 35487, USA
[c] Department of Physics and Astronomy, University of Alaska Anchorage, 3211 Providence Dr., Anchorage, AK 99508, USA
[d] CTSPS, Clark-Atlanta University, Atlanta, GA 30314, USA
[e] School of Physics and Center for Relativistic Astrophysics, Georgia Institute of Technology, Atlanta, GA 30332, USA
[f] Department of Physics, Southern University, Baton Rouge, LA 70813, USA
[g] Department of Physics, University of California, Berkeley, CA 94720, USA

0168-9002/$ - see front matter
doi:10.1016/j.nima.2010.03.102

[h] Lawrence Berkeley National Laboratory, Berkeley, CA 94720, USA
[i] Institut für Physik, Humboldt-Universität zu Berlin, D-12489 Berlin, Germany
[j] Fakultät für Physik & Astronomie, Ruhr-Universität Bochum, D-44780 Bochum, Germany
[k] Physikalisches Institut, Universität Bonn, Nussallee 12, D-53115 Bonn, Germany
[l] Université Libre de Bruxelles, Science Faculty CP230, B-1050 Brussels, Belgium
[m] Vrije Universiteit Brussel, Dienst ELEM, B-1050 Brussels, Belgium
[n] Department of Physics, Chiba University, Chiba 263-8522, Japan
[o] Department of Physics and Astronomy, University of Canterbury, Private Bag 4800, Christchurch, New Zealand
[p] Department of Physics, University of Maryland, College Park, MD 20742, USA
[q] Department of Physics and Center for Cosmology and Astro-Particle Physics, Ohio State University, Columbus, OH 43210, USA
[r] Department of Astronomy, Ohio State University, Columbus, OH 43210, USA
[s] Department of Physics, TU Dortmund University, D-44221 Dortmund, Germany
[t] Department of Subatomic and Radiation Physics, University of Gent, B-9000 Gent, Belgium
[u] Max-Planck-Institut für Kernphysik, D-69177 Heidelberg, Germany
[v] Department of Physics and Astronomy, University of California, Irvine, CA 92697, USA
[w] Laboratory for High Energy Physics, École Polytechnique Fédérale, CH-1015 Lausanne, Switzerland
[x] Department of Physics and Astronomy, University of Kansas, Lawrence, KS 66045, USA
[y] Department of Astronomy, University of Wisconsin, Madison, WI 53706, USA
[z] Department of Physics, University of Wisconsin, Madison, WI 53706, USA
[aa] Physical Sciences Laboratory, University of Wisconsin, Madison, WI 53706, USA
[ab] Institute of Physics, University of Mainz, Staudinger Weg 7, D-55099 Mainz, Germany
[ac] Université de Mons, 7000 Mons, Belgium
[ad] Bartol Research Institute and Department of Physics and Astronomy, University of Delaware, Newark, DE 19716, USA
[ae] Department of Physics, University of Oxford, 1 Keble Road, Oxford OX1 3NP, UK
[af] Department of Physics, University of Wisconsin, River Falls, WI 54022, USA
[ag] Oskar Klein Centre and Department of Physics, Stockholm University, SE-10691 Stockholm, Sweden
[ah] Department of Astronomy and Astrophysics, Pennsylvania State University, University Park, PA 16802, USA
[ai] Department of Physics, Pennsylvania State University, University Park, PA 16802, USA
[aj] Department of Physics and Astronomy, Uppsala University, Box 516, S-75120 Uppsala, Sweden
[ak] Department of Physics and Astronomy, Utrecht University/SRON, NL-3584 CC Utrecht, The Netherlands
[al] Department of Physics, University of Wuppertal, D-42119 Wuppertal, Germany
[am] DESY, D-15735 Zeuthen, Germany

ARTICLE INFO

Article history:
Received 4 March 2010
Accepted 6 March 2010
Available online 18 March 2010

Keywords:
PMT
Neutrino
Cosmic rays
Ice
Cherenkov

ABSTRACT

Over 5000 PMTs are being deployed at the South Pole to compose the IceCube neutrino observatory. Many are placed deep in the ice to detect Cherenkov light emitted by the products of high-energy neutrino interactions, and others are frozen into tanks on the surface to detect particles from atmospheric cosmic ray showers. IceCube is using the 10-in. diameter R7081-02 made by Hamamatsu Photonics. This paper describes the laboratory characterization and calibration of these PMTs before deployment. PMTs were illuminated with pulses ranging from single photons to saturation level. Parameterizations are given for the single photoelectron charge spectrum and the saturation behavior. Time resolution, late pulses and afterpulses are characterized. Because the PMTs are relatively large, the cathode sensitivity uniformity was measured. The absolute photon detection efficiency was calibrated using Rayleigh-scattered photons from a nitrogen laser. Measured characteristics are discussed in the context of their relevance to IceCube event reconstruction and simulation efforts.

1. Introduction

IceCube [1,2] is a kilometer-scale high energy neutrino telescope currently under construction at the geographic South Pole. A primary goal is to detect high energy neutrinos from astrophysical sources, helping to elucidate the mechanisms for production of high energy cosmic rays [3].

IceCube uses the 2800 m thick glacial ice sheet as a Cherenkov radiator for charged particles, for example those created when cosmic neutrinos collide with subatomic particles in the ice or nearby rock. Neutrino interactions can create high energy muons, electrons or tau particles, which must be distinguished from downgoing background muons based on the pattern of light emitted. The Cherenkov light from these particles is detected by an embedded array of Digital Optical Modules (DOMs), each of which incorporates a 10 in. diameter R7081-02 photomultiplier tube (PMT) made by Hamamatsu Photonics. The DOMs transmit time-stamped digitized PMT signal waveforms to computers at the surface.

The finished array will consist of 4800 DOMs at depths of 1450–2450 m, deployed at 17 m intervals along 80 vertical cables, which in turn are arranged in a triangular lattice with a horizontal spacing of approximately 125 m. An additional 320 DOMs will be frozen into 1.8 m diameter ice tanks located at the surface to form the IceTop array, which is designed for detection of cosmic ray air showers. The geometrical cross-sectional area will be $\sim 1\,\mathrm{km}^2$ and the volume of ice encompassed will be $\sim 1\,\mathrm{km}^3$. Another 360 DOMs will be deployed in a more compact geometry ("Deep Core" [4]) using PMTs almost identical to those described here but with a higher efficiency photocathode.

* Corresponding authors. Tel.: + 608 890 0577.
E-mail addresses: mase@hepburn.s.chiba-u.ac.jp (K. Mase), chris.wendt@icecube.wisc.edu, chwendt@icecube.wisc.edu (C. Wendt), syoshida@hepburn.s.chiba-u.ac.jp (S. Yoshida).

[1] Affiliated with Universität Erlangen-Nürnberg, Physikalisches Institut, D-91058 Erlangen, Germany.
[2] On leave of absence from Università di Bari and Sezione INFN, Dipartimento di Fisica, I-70126 Bari, Italy.
[3] Affiliated with School of Pure and Applied Natural Sciences, Kalmar University, S-39182 Kalmar, Sweden.
[4] NASA Goddard Space Flight Center, Greenbelt, MD 20771, USA.

In this paper we describe measurements characterizing and calibrating IceCube PMTs, and discuss their relevance to detector performance and event reconstruction. First we describe the signals of interest in Section 2. Section 3 briefly describes the DOMs in which IceCube PMTs are deployed. Section 4 describes selection and basic features of the PMT, including the dark noise rate. Section 5 presents the design of the HV divider circuit. Sections 6–9 discuss characteristics of the PMT in the photon counting regime, starting with single photon waveforms and charge distributions. Time resolution is studied with a pulsed laser system. Uniformity of the photon detection response on the photocathode area is measured by scanning the entire cathode surface with a UV LED. Absolute efficiency calibration of the IceCube PMTs is carried out using Rayleigh-scattered light from a calibrated laser beam. Sections 10–11 describe response to bright pulses of light, including saturation behavior and afterpulse characteristics.

2. Characteristics of optical signals in IceCube

We begin by summarizing what the PMTs are supposed to detect, namely the optical signals generated by neutrinos in IceCube [1,2]. Of particular relevance are the amplitudes and widths of the pulses, requirements on time resolution, and how the pulses are used to reconstruct physics events or reject backgrounds.

In detection of a high energy ν_μ by IceCube, the neutrino interaction creates a muon that traverses kilometers of ice and generates Cherenkov light along its path. Above 1 TeV, the muon loses energy stochastically to produce multiple showers of secondary particles, resulting in an overall light yield proportional to the muon energy [5,6]. Most light is emitted near the Cherenkov angle, which is 41° away from the track direction. The arrival times of detected photons depend on the position of each DOM relative to the muon's path. For close DOMs, most photons arrive in a pulse less than 50 ns wide, in which the earliest photons have traveled straight from the muon track without scattering. Significant scattering accumulates along photon trajectories with a characteristic length scale of about 25 m [7], so light pulses lengthen with distance and reach 1 μs (FWHM) for DOMs 160 m away from a muon track. Depending on primary energy and distance from the track, each PMT can see single photons or pulses ranging up to thousands of photons.

Event reconstruction [1,2,8] builds on principles established for the predecessor array, AMANDA [9,10]. The observed PMT waveforms from individual DOMs are correlated and built into events, which are fitted to physics hypotheses using the maximum likelihood method. Each fit has access to the complete pattern of light amplitude and timing seen by the DOMs, and accounts for the DOMs' time response and optical sensitivity as well as time dispersion and optical attenuation introduced by the ice. The fit gives the direction and energy of the muon, which in turn characterizes its parent neutrino.

The observed light pattern is also used to distinguish the rare neutrino events from the large background of muons created in cosmic ray air showers, which are 10^6 times more numerous. For this the reconstructed direction is key, because neutrinos can come from any direction, even up from below, but the background muons are downgoing. A small fraction of background events can be misreconstructed in direction, thereby appearing to come from neutrinos, but the pattern of detected light will generally be a poor match compared to expectations for a properly reconstructed track. Misreconstruction can be aggravated by additional muons from the same shower or other coincident showers. This separation between signal and background is accomplished by evaluating relative probabilities on an event-by-event basis, and is aided by good time and amplitude resolution as well as by low PMT noise rates.

Similar principles apply to other types of high energy neutrino interaction. Instead of a muon, an electron can be created that loses its energy in a few-meter-long particle shower [11]; on the scale of IceCube, such a shower appears almost like a point source of Cherenkov light. For a sufficiently energetic neutrino, the light can be detected hundreds of meters away, and nearby DOMs can see enough light to drive their PMTs into the nonlinear saturation regime. Therefore proper modeling of saturation behavior is needed for good reconstruction and background rejection.

Design studies [2] for important physics goals have shown that sufficient reconstruction quality is achieved for a PMT timing resolution of 5 ns, low-temperature noise rate below 500 Hz, and effective dynamic range of 200 photoelectrons per 15 ns.

In the case of lower energy (MeV) neutrinos from supernovae, IceCube cannot resolve individual interactions. Instead, supernovae would be detected as a momentary increase in the collective photon counting rate for the whole array, corresponding to a large number of neutrino interactions within a few seconds. The dark noise rate of the PMTs is particularly important here, because it dictates the statistical significance of any excess count rate.

IceTop uses DOMs identical to those in the deep ice. Here the signals arise from muons, electrons and gamma rays in cosmic ray air showers [12]. These particles deposit energy in the ice tanks housing the DOMs, resulting in light pulses up to several hundred nanoseconds long. The arrival times and amplitudes in the surface array are then used to reconstruct the shower core position, direction, and energy. An overall timing resolution of 10 ns provides pointing accuracy of about 1°. The PMT pulses range from single photoelectrons at the periphery of showers to 10^5 photoelectrons for a 1 EeV shower that strikes within the array. To achieve the implied dynamic range, each tank contains two DOMs operating at gains differing by a factor 50.

3. The IceCube optical detector: DOM

The Digital Optical Module is the fundamental element for both optical detection and data acquisition in IceCube [2,13,14]. It contains a 10 in. diameter PMT supported by coupling gel, the PMT high voltage generator and divider circuits, an LED flasher board used for calibration of the array geometry and study of ice properties, and the DOM mainboard which contains the analog and digital signal processing electronics [14]. The PMT is surrounded by a μ−metal grid to shield it from the terrestrial magnetic field and improve the PMT performance. All systems are housed within a pressure sphere made of 0.5 in. thick glass, capable of withstanding pressures to 70 MPa. The glass and gel set the short wavelength cutoff of the DOM at about 350 nm, where the PMT by itself is still relatively efficient.

Strings of DOMs are deployed into water columns that have been melted by a hot-water drill. After refreezing, DOMs are optically well coupled to the surrounding glacial ice. Signal and power connections between the DOMs and the surface are provided by copper twisted-pair wires bundled together to form the main cables. PMT signals are digitized on the mainboard, buffered in memory, and sent to the surface upon command of surface readout processors.

4. PMT selection and dark noise rate

A number of large-area PMTs are commercially available and have been used successfully to instrument large volumes in other

experiments. IceCube selected the R7081-02 made by Hamamatsu Photonics, emphasizing the criteria of low dark noise and good time and charge resolution for single photons. Some manufacturer's specifications are shown in Table 1, and more detailed measurements are described in the following.

The nominal gain of 10^7 was chosen to give single photon pulses around 8 mV, which is well above the digitizer precision and other electronic noise levels (both ~ 0.1 mV). Aging was not a concern for gain selection, since at the expected noise rates, the corresponding total charge delivered by each deep-ice PMT will be less than 1 C after 20 years (or 100 C for IceTop). Tubes with 10 and 12 stages were evaluated, with the 10 stage options showing a better peak-to-valley ratio at this gain. Lower gains of 5×10^6 and 10^5 were chosen for IceTop PMTs because air shower pulses generally comprise many photon detections.

The R7081-02 has 10 linear focused dynode stages and achieved the nominal gain of 10^7 at about 1300 V in our tests with the recommended divider ratios (observed range 1050–1600 V for 3744 PMTs). Its 10 in. diameter photocathode is composed of the standard bialkali material (Sb–Rb–Cs, Sb–K–Cs) with a peak quantum efficiency of approximately 25% at 390 nm. With a borosilicate glass envelope, the spectral response [16] is a good match to the spectrum of Cherenkov light after propagation through ice [7], especially considering the 350 nm cutoff of the housing.

In response to IceCube requirements, the supplied R7081-02 units were manufactured with a custom low radioactivity glass. The resulting dark count rate at low temperatures is close to 300 Hz in the -40 to -20 °C range of greatest interest for IceCube (Fig. 1). The higher room temperature rate can be attributed mostly to cathode thermionic emission, which is suppressed at low temperature. The low temperature rate is believed to be dominated by radioactive decays plus scintillation in the PMT glass envelope, and shows a rise with decreasing temperature similar to that reported in other studies [17]. The association of this rate with decays is supported by time correlations observed on scales up to 1 ms, as can result from delayed particle capture or de-excitation of states created by decays. It is also supported by the observed effect of taping: for these measurements, the entire outside surface of the PMT glass was covered in black vinyl tape, pulled tightly against the glass to avoid bubbles. The taping is observed to reduce the low-temperature noise rate by about half. The reduction is attributed to absorption of outward going decay photons, which can otherwise be channeled to the photocathode via internal reflection. The taped result is appropriate for PMTs installed in IceCube DOMs because they are optically coupled to gel (then glass and ice) where the refractive index matches better than it does for air.

The low dark rate allows IceCube to record all events that satisfy simple multiplicity conditions, and is particularly important for observation of any galactic supernova event. Such a supernova could yield about 10^6 excess photon counts in IceCube over a few seconds [18]. The single-PMT dark rate, multiplied by the number of PMTs, contributes a background rate of 1.5×10^6 Hz, with a similar contribution from decays in the DOMs' glass housing. The excess from a supernova would be easily observed above this background, even including the details of its time structure.

Table 1
Hamamatsu specifications for the R7081-02 PMT (typical) [15].

Spectral response	300–650 nm
Quantum efficiency at 390 nm	25%
Supply voltage for gain 10^7	1500 V
Dark rate at -40 °C	500 Hz
Transit time spread	3.2 ns
Peak to valley ratio for single photons	2.5
Pulse linearity at 2% deviation	70 mA

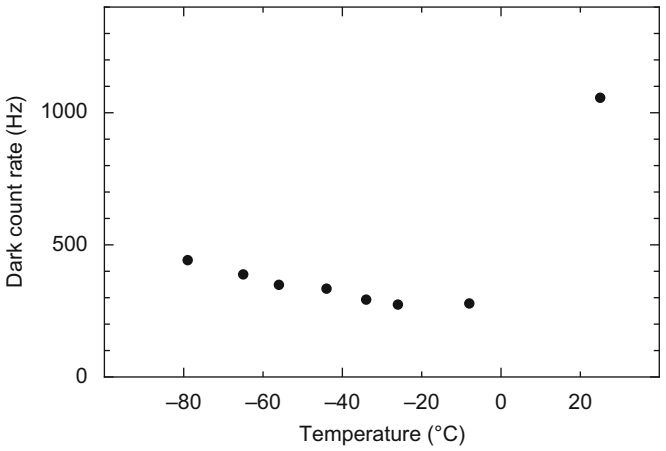

Fig. 1. Dark count rate versus temperature for a sample IceCube PMT covered with black tape (see text). Rates were recorded after a settling time of 12 h of dark operation at gain 10^7 and discriminator threshold 0.25 times the single photoelectron peak. An artificial deadtime circuit rejected additional hits within 6 μs of each count, including about half of all afterpulses (Section 11). The contribution from cosmic rays (< 5 Hz) has not been subtracted.

On the other hand, a high energy neutrino event creates optical pulses distributed over 3 μs, with most information contained within a time window less than 300 ns wide in each DOM. Because this window is so short, the low PMT dark rate implies that only 1% of muons would be accompanied by a relevant noise count among the 100 DOMs closest to the track, and many of these DOMs detect multiple signal photons. Therefore the degradation of reconstruction and background rejection is very small. The dark noise rate has even less effect for IceTop DOMs, due to higher thresholds and coincidence requirements.

5. High voltage divider circuit

The relative dynode voltage ratios for R7081-02 have been optimized by Hamamatsu to achieve a maximum collection efficiency while achieving 10^7 gain between 1050 and 1600 V. Our high voltage subsystem design fulfills the additional requirements of low power consumption, long-term reliability, and sustained response to very bright pulses lasting up to a microsecond.

The dynode voltages are provided by a passive resistive divider with a total resistance of 130 MΩ (Fig. 2). The rather high total resistance is chosen to minimize power consumption, which is an important economic consideration for operations at the South Pole. A custom, compact, high voltage generator [19] that is both low power (< 300 mW) and low noise (< 1 mV ripple, peak-to-peak) is used in conjunction with the passive divider.

Capacitors are placed across the last six dynode intervals and between the last dynode and anode. These capacitors help sustain the PMT output for large pulses of up to 10^6 photoelectrons (p.e.). Even for illumination in the PMT saturation region (~ 200 p.e./ns, see Section 10), the transient gain loss after a 1 μs pulse (2×10^5 p.e.) is observed to be less than 1%. A detailed simulation [20] indicates that such a pulse could arise from a 50 PeV electron shower 100 m away from the PMT, which would then be faithfully recorded. Pulses up to five times this large (10^6 p.e.) still result in less than 20% transient gain loss, so while the primary pulse would be completely saturated, afterpulse amplitude could be used to estimate the total illumination (Section 11). Finally above

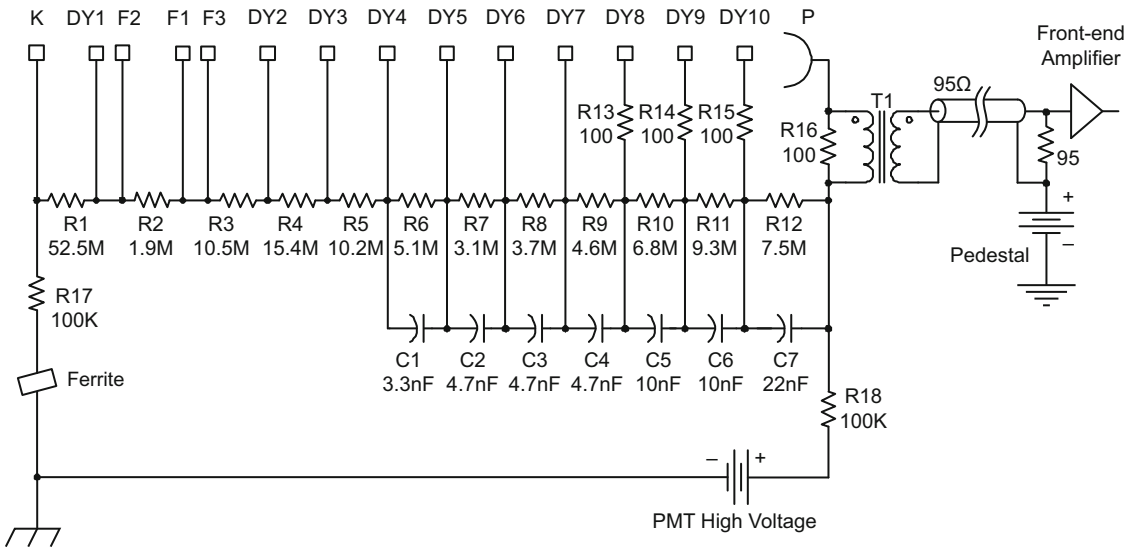

Fig. 2. Schematic of the passive HV divider circuit, shown with coupling to the front-end amplifier on the digitizer board.

2×10^7 p.e. the gain loss rises rapidly above 50%. For all these transient gain losses, recovery occurs within the RC time constants of order 1 s.

Low-inductance resistors (100 Ω, R13 through R15) are used to dampen ringing that arises from coupling of the larger dynode filter capacitors with parasitic inductance in the dynode leads and printed circuit traces. This ringing could otherwise be a nuisance when reconstructing a single PMT output waveform as a series of photon hits.

The IceCube PMTs are operated with their cathode at ground potential. Therefore the high voltage anode is AC coupled to the front-end amplifiers. For the AC coupling, we use a custom bifilar-wound 1:1 toroidal transformer rather than a DC blocking capacitor. High voltage reliability is achieved in the transformer winding using wire with insulation rated for over 5 kV DC. The resulting stray capacitance from anode to front-end amplifier is only 30 pF, which limits the stored energy which might damage the analog front-end if sparking should occur in the HV system. In contrast, a coupling capacitor large enough to meet the signal droop specification would be at least 1000 times larger than the stray capacitance of the transformer. The transformer topology also reduces noise by avoiding noisy high voltage ceramic signal coupling capacitors and by breaking a ground loop path involving the HV power supply. The ferrite and resistors in series with the HV supply further reduce coupling of high frequency noise to the front end input.

The transformer coupling delivers good signal fidelity for single-photoelectron (SPE) waveforms with risetimes of a few ns, while transmitting wide pulses exceeding 1 μs with less than 10% droop and undershoot. The custom design uses 18 bifilar turns on a ferrite (Magnetics Type H) toroid core, providing roughly flat coupling from 8 kHz to over 100 MHz at operating temperatures down to −40 °C. The self-resonant frequency is above 150 MHz. The low operation temperature presented a challenge because the permeability of the transformer core decreases rapidly with temperature, leading to a shorter droop time constant. Although most DOMs have a time constant around 15 μs at ambient temperatures near −30 °C, 1200 DOMs were built using an older transformer design yielding a time constant around 1.5 μs at −30 °C. The improved performance of the new design was achieved with a larger core and more turns, at the expense of a slightly wider SPE pulse shape (Fig. 3). The two designs are deployed intermixed.

The droop and undershoot are relevant for the μs long trains of photon pulses expected in DOMs over 100 m away from high

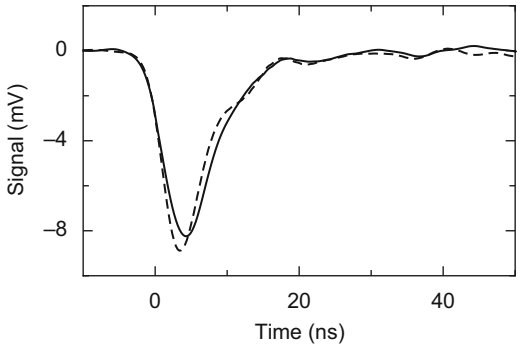

Fig. 3. Average of 10,000 SPE waveforms for one PMT at gain 1×10^7, as seen at the secondary of the AC coupling transformer. Results for other PMT samples are very similar. The solid and dashed curves correspond to new and old transformer designs discussed in Section 5.

energy events, such as 10 TeV electron showers or 500 TeV muon tracks. The small remaining effects are corrected by a software digital filter as a first step in event reconstruction, based on individual time constants for each DOM. The residual error is typically less than 1% of the pulse amplitude (except for pulses with peak or undershoot outside the ADC dynamic range, which is limited after 400 ns [14]).

The divider circuit is constructed on a 10 cm-diameter printed circuit board which is directly solder-mounted to the PMT. All components (except R13–R16) are through-hole mount type, selected with a voltage derating factor of two or greater (typically four) to ensure long-term reliability. Strict voltage and voltage gradient rules are applied to the board layout.

Coaxial cables are used for the connections to the high voltage generator and the front end amplifier on the digitizer board. The effective load for anode output pulses is 50Ω (43Ω for the older transformer design), which includes a back-termination resistor on the primary side of the transformer (R16), the transformer AC response, and the input impedance of the amplifier.

6. Single photoelectron waveform and charge

The SPE waveform shape and charge probability distribution are important for event reconstruction. The DOM waveform

digitizers are triggered when the signal reaches about 0.25 times the typical SPE peak amplitude, after which the PMT output waveform is digitized for up to 6.4 μs. The detection efficiency for single photons depends directly on the fraction of the SPE charge distribution above trigger threshold. For high energy neutrino events, many waveforms show contributions from multiple photons, all of which could provide useful information during event reconstruction. The overall light yield provides an estimate of the neutrino energy, and the space and time distribution of light helps to reconstruct direction and reject backgrounds. The time distribution of photons can be extracted from each PMT waveform if the response to single photons is well understood. The response to each photon is approximately given by the average SPE waveform, scaled randomly according to the complete charge probability distribution.

In order to mimic the ambient temperature in the ice, PMTs were placed in a freezer box at −32 °C and illuminated by diffused light from a 375 nm UV LED. The light was generated in 10 ns pulses with intensity of about 0.1 photons per shot (~ 0.02 photoelectrons per shot), dim enough to initiate only SPE signals. Fig. 3 shows the average SPE waveform, measured at the output of the AC coupling transformer with a digital storage oscilloscope (LeCroy LT374, 500 MHz bandwidth, 0.5 ns samples). Here the 95 Ω input impedance of the DOM's front end amplifier was replaced by the series combination of a 50 Ω resistor and the oscilloscope input.

Individual waveforms have different amplitudes but their shapes are similar to within a few percent. The waveform is dominated by a peak of Gaussian shape ($\sigma = 3.2$ ns) which accounts for 83% of the area. A tail on the late side of the peak accounts for the remaining area and exhibits a small amount of ringing. About 90% of the charge is collected before 10 ns after the peak. A substantial part of the observed pulse width is attributed to the damping resistors and the coupling transformer (Section 5).

To study the total charge in SPE events, a computer-controlled integrating ADC module (LeCroy 2249A) was used to integrate charge in a 70 ns window, triggered by the synchronization signal of the LED pulse generator. Fig. 4 shows a typical charge histogram, which exhibits a clear SPE peak to the right of the pedestal peak. The Gaussian part of the SPE peak corresponds to a charge resolution of approximately 30%.

The non-Gaussian component rising below 0.3 times the SPE charge in Fig. 4 has been studied to verify that such small pulses actually reflect in-time detection of photons, and not accidental coincidences of noise pulses such as from thermionic emission at the dynodes. The check for a noise contribution was done with the LED light output disabled (but not the synchronization signal that triggers acquisitions); all counts outside the narrow pedestal region were greatly suppressed compared to Fig. 4.

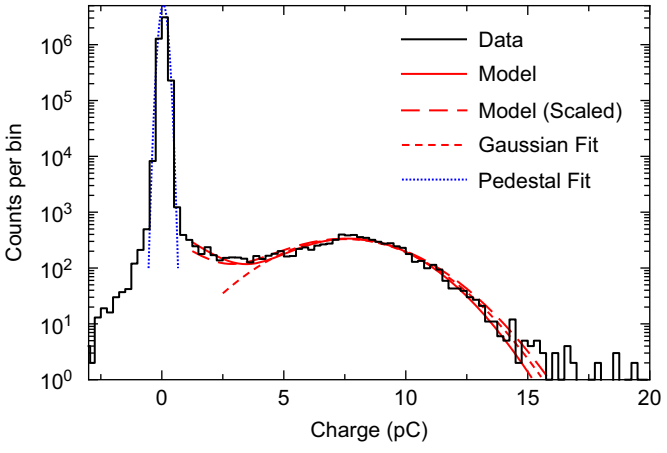

Fig. 4. Typical pedestal-subtracted SPE charge histogram at gain 5×10^7, including pedestal peak. Fits refer to Eq. (1), with the constraint $q_\tau/q_0 = 0.2$. The remaining parameters are optimized to fit this histogram for the curve labeled "Model", while "Model (Scaled)" optimizes only the scale parameter q_0 while holding σ_q/q_0 and P_e at values that describe the average of 120 PMTs.

The low-charge component has been described in the past for many PMTs [21], and has been attributed to a sizable probability for backscattering of the primary photoelectron at the first dynode [22,23], leading to events where only a few secondaries are produced instead of the usual 10–20.

The shape of the low-charge component is important because even small pulses below the DOM's trigger threshold will be recorded in events with multiple photoelectrons. Therefore event reconstruction should account for the entire charge probability distribution down to zero charge, which we model as a Gaussian plus an exponential term [21]:

$$f(q) = \frac{P_e}{q_\tau}\exp\left[-\frac{q}{q_\tau}\right] + (1-P_e)\frac{1}{\sqrt{2\pi}\sigma_q}\exp\left[-\frac{(q-q_0)^2}{2\sigma_q^2}\right]. \quad (1)$$

Here P_e is the fraction of events in the low-charge exponential part, q_0 is the charge at the SPE peak which defines the PMT gain, σ_q is the width of the Gaussian fit around the SPE peak, and q_τ is the decay constant in the exponential component. Fig. 4 shows that this is a good model for the shape of the charge histogram away from the pedestal.

Fig. 5 shows results of fitting equation (1) for a large sample of PMTs at different gains above 5×10^7, excluding the very low charge region $q < 0.15q_0$ and the very high charge region more than 2σ past the peak. The value of q_τ/q_0 is substantially degenerate with P_e for describing observed spectra in the fitted range, so it has been fixed at the representative value of 0.20. The scaled quantities σ_q/q_0, q_τ/q_0, and P_e are found not to vary strongly with the PMT gain. The very small pulses with $q < 0.15q_0$ were omitted to avoid confusion with the tail of the pedestal distribution; results were the same if the low-charge cut was moved to $0.25q_0$. The charge resolution σ_q/q_0 has been separately studied for gains between 10^7 and 10^8 and again no significant variations were seen.

Fig. 5 also shows the spread in parameters from PMT to PMT. The distribution in each parameter is approximately Gaussian,

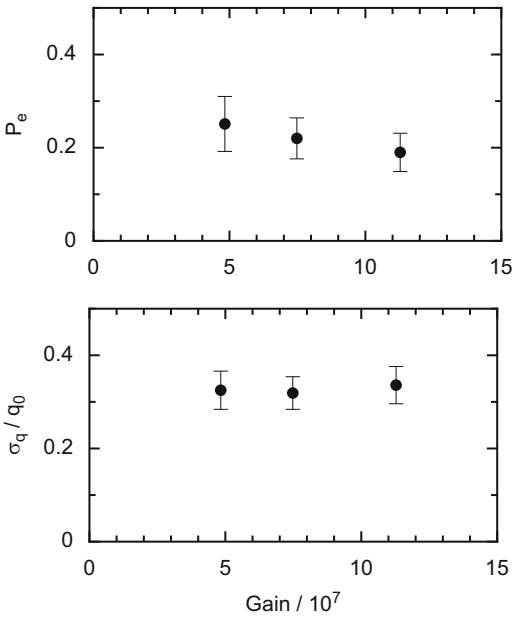

Fig. 5. Scaled parameters from Eq. (1) as a function of PMT gain. The error bars show the 1σ spread in parameters obtained for a sampling of 115 PMTs.

with the width shown by the error bars. The spread is substantial, but is not expected to have a large effect on data analysis, so the IceCube PMTs do not need to be parameterized individually. Instead, an average model is currently used in event simulation and reconstruction, without modeling the spread. The similarity among PMTs can also be gauged from Fig. 4, where data from one PMT is compared with a model curve scaled from the average fit results for 120 PMTs.

The above measurements were performed with diffuse light and represent an average over the photocathode surface. In a separate measurement at gain 10^7, substantial differences were observed as a function of position; for example, the peak-to-valley ratio decreased to near unity close to the edge of the photocathode, compounding the effects of gain variation (Section 8).

7. Time resolution

The timing of recorded SPE waveforms, relative to the photon arrival time, was studied at −40 °C using fast pulses (FWHM 50 ps) from a Hamamatsu PLP-10 diode laser. Pulses were optically attenuated and diffused over the PMT face, yielding an average of 0.04 photoelectrons per shot. The wavelength was 405 nm.

Each PMT was set for gain 10^7 based on its SPE charge spectrum. Hits greater than 0.4 times the SPE charge were recorded using the DOM digitization and readout electronics. Synchronization pulses from the laser were also digitized to indicate the true photon arrival times to within a fixed offset. Hit times were defined as the points where each waveform reached 50% of its maximum, resulting in the time resolution histogram of Fig. 6.

The main peak of the time histogram has width equivalent to a Gaussian of $\sigma = 2.0$ ns, although the rising and falling edges of the peak fit better to half-Gaussians with $\sigma = 1.2$ and 2.7 ns, respectively. Some of the width can be attributed to simultaneous illumination of the entire photocathode in our tests. When illuminated at the center only, the width decreased to 1.5 ns; conversely, the outer 3 cm of the photocathode exhibited additional delay of about 3 ns and additional broadening. The data acquisition system contributed a time smearing of less than 0.6 ns, which has not been subtracted.

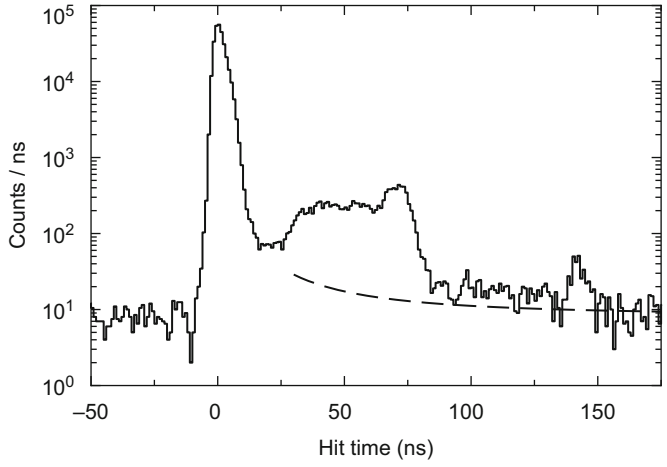

Fig. 6. Typical distribution of SPE hit times for an IceCube PMT, when illuminated by narrow pulses from a diode laser. Counts are shown for 1 ns time bins, referenced to a laser synchronization pulse. A small fraction of late pulses (dashed line) are due to laser afterglow plus the random background count rate; hit fractions described in the text are corrected accordingly. The random background also explains the counts before the synchronization pulse.

About 4% of hits are found in a shoulder (25–65 ns) and secondary peak at 71 ns, and 0.2% make up a corresponding tertiary structure (85–160 ns). The delayed hits are believed to arise when an electron trajectory is scattered back from the first dynode towards the photocathode, where it turns around and then eventually arrives back at the first dynode to initiate the pulse [23–25].

Because of strong photon scattering in the ice, the dispersion of hit times by the PMT at the 2 ns scale is not a limiting factor for reconstruction in IceCube; likewise for the tail at late times. Considering the spacing between DOMs, photons must typically travel tens of meters before detection, which is comparable to the scattering length of around 25 m [7]. A detailed simulation of photon scattering [26] showed that at 10 m distance, about 40% of photons are delayed by more than 5 ns, and 10% of photons are delayed between 20 and 80 ns. This is larger than the corresponding effects from the PMT itself. On the other hand, DOMs close to a high energy track can be expected to detect at least one photon with negligible delay, and then the very small 1.2 ns dispersion on the early side of the time resolution peak may be relevant when reconstructing arrival time of the earliest photon or the pulse rise time.

The time resolution study also reveals DOM-to-DOM differences in the nominal delay of SPE waveforms relative to photon arrival time. This delay includes PMT transit time plus signal delays between the PMT output and the digitizer. The PMT transit time is found to vary according to the square root of the applied voltage,

$$T_{transit}(V_{PMT}) = T_0 + 2\kappa V_0\sqrt{V_0/V_{PMT}} \quad (2)$$

where $\kappa = 0.017$ ns/V is the slope at $V_0 = 1500$ V. The voltage applied to each PMT is set for a design gain 10^7, which is achieved between 1050 and 1600 V in 99.9% of PMTs. The resulting RMS spread of the overall time offset is 2.7 ns. We find 5% of DOMs more than 5 ns away from the mean, so the DOM-to-DOM corrections are currently included in reconstruction.

8. Two-dimensional photocathode scan

The number of photons arriving at the PMT is calculated from the observed photoelectron signals via the PMT optical efficiency. This is separated into an overall "absolute efficiency" and an angular dependence. The dominant factor in angular dependence is just the amount of photocathode area which can be seen from various directions. However, this has to be adjusted for the fact that the photocathode surface is very large and different portions do not all yield the same efficiency.

We have systematically analyzed the variation of efficiency with photocathode position at 25 °C, using a two-dimensional scan system. A UV LED (370 nm) with collimator produced a 1 mm spot which was moved along the curved PMT surface, maintaining normal incidence of the light. The LED delivered approximately 125 photons per 80 ns pulse. The anode voltage was set for gain 10^7 at the center of the photocathode, as measured by the SPE charge peak (q_0 in Eq. (1)). The PMT pulse charge for each position was then measured by an integrating ADC triggered by the LED pulser.

Fig. 7 shows typical response maps on the cathode surface. The measured charge is proportional to the net photomultiplier efficiency and reflects the combined position dependence of photocathode quantum efficiency, collection efficiency, and dynode multiplication. PMT to PMT variation of the efficiency at a given spot on the photocathode may be as great as 40%, however, the spread in the area-integrated efficiency from PMT to PMT is much smaller, of order 10% (see Section 9). The average

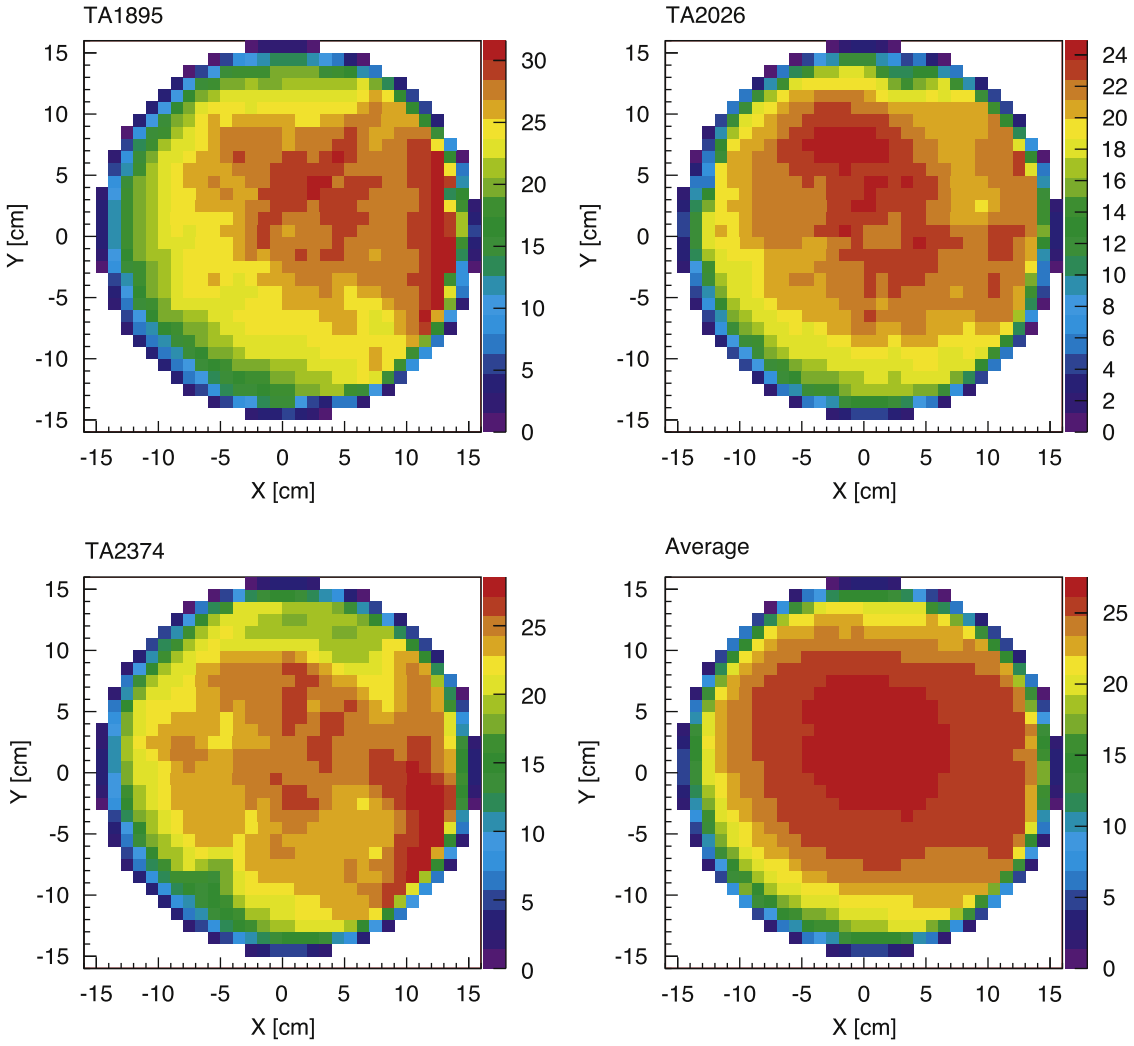

Fig. 7. Position dependence of the light pulse response for three example PMTs, and the average of 135 PMTs (lower right). The *X*–*Y* coordinates measure distance from the center of the photocathode along the curved PMT face. The value at each *X*–*Y* position indicates the PMT output pulse charge in units of the SPE charge, averaged over many pulses.

map shows a uniform falloff in the edge region, except for a small bias in the +*X* direction. All PMTs were measured in the same orientation, so this bias could be associated to the first dynode position or the geomagnetic field.

A small part of the variation seen in the scans can be attributed to systematic errors, which arise mainly from the geomagnetic field and LED luminosity variance. The geomagnetic field of 462 mG is attenuated by about 50% with a shield made of μ- metal sheet and wire, as also used in IceCube DOMs. By comparing measurements with the PMT rotated from its standard orientation in various ways, we determined the field's effect on the efficiency variation is about 10%. Because the magnetic shield is the same, the overall results are representative of what is expected for deployed IceCube DOMs. (The field at the South Pole is 553 mG, and more vertical relative to the PMT axis.) The time dependence of LED luminosity affected the shape of each scan by less than 2%, as seen by reproducibility of the scan results.

By reducing the light intensity to give only SPE hits, a similar map has been constructed for gain variation. The gain can vary as a function of position because the corresponding photoelectron trajectories arrive differently at the first dynode, leading to different yields of secondary electrons. The observed gain (defined by q_0 in Eq. (1)) varies within $\pm 10\%$ over the active region when high voltage is set for gain 5×10^7 at the center. However, the low-charge contribution to the SPE charge spectrum (P_e in Eq. (1)) was found to also vary with position, so that the peak-to-valley ratio decreases close to unity near the edge of the photocathode. In this way, the average charge delivered per photoelectron was observed to decrease by up to 30% at nominal gain 10^7. Because of these effects, the detection efficiency map for single photons using a specific discriminator threshold can differ somewhat from the maps of Fig. 7.

The integrated sensitivity for a broad beam of photons incident from a particular direction follows from the cathode efficiency maps by averaging over the surface seen from that direction [27], with correction for non-normal incidence on surface elements as appropriate [28]. For this purpose the relative efficiency map is assumed not to vary with wavelength, i.e., each position is assumed to obey the spectral response curve given by the manufacturer [16]. The averaging substantially reduces the effect of variations over the surface so the sensitivity is not strongly dependent on direction at moderate polar angles. Only light that arrives at large polar angles relative to the PMT axis will primarily illuminate the equator region and therefore show strong azimuthal dependence. Likewise, the variation in charge spectrum from center to edge has little effect after averaging.

The scans were performed on a small fraction of the IceCube PMTs, so only the average variation with polar angle is used in

simulation and reconstruction. For IceCube, the remaining PMT-to-PMT variation in directional sensitivity has very small consequences, because light is typically scattered after traveling about 25 m through the ice, and additional scattering takes place in the refrozen ice in the hole where the DOMs are deployed. The PMT-to-PMT variation, as well as the position dependence itself, could be more important for detectors deployed in water where scattering lengths are much longer [29].

9. Absolute efficiency calibration

The absolute calibration of PMT optical efficiency is important because IceCube uses the observed number of photons to estimate energy in reconstructed neutrino interactions. Showers initiated by electrons or tau leptons yield light in proportion to the energy, and so do muons above 1 TeV where energy loss is dominated by direct pair production, photonuclear interactions and bremsstrahlung [5,6].

Optical efficiency can be studied after deployment by using light from muons (produced in cosmic ray showers above IceCube) or from calibrated beacons deployed in the ice nearby. However, it is hard to isolate the PMT response from the effects of light scattering and attenuation in the ice, which have some uncertainties [7].

Here we describe the laboratory calibration of standard PMTs installed in 16 IceCube DOMs distributed throughout the array. The calibrated PMTs provide direct information for the energy calibration of IceCube, and will also help clarify the ice effects in other studies, which is an important subject on its own.

9.1. Technique

Our setup for measuring a PMT's UV photon detection efficiency is shown in Fig. 8. A pulsed 337 nm laser beam is passed through a chamber containing pure nitrogen gas, and the PMT to be calibrated is illuminated by the tiny amount of light that is Rayleigh scattered at about 90° from the beam. The PMT is rotated inside the dark box to probe different positions on the photocathode surface. The primary beam intensity is measured with a calibrated silicon photodiode "energy probe", and sets the fundamental scale for our efficiency measurement. A pressure gauge and temperature sensor provide the gas density. Beam intensity, geometry and gas density are then folded with the well-known Rayleigh scattering cross-section to obtain the absolute number of photons per pulse incident on the PMT. Individual photon detections are counted in each pulse and divided by the number incident to obtain the optical sensitivity at 337 nm. Additional corrections (Section 9.4) are needed to obtain DOM efficiency at wavelengths around 400 nm where IceCube is most sensitive.

The measurement combines effects of quantum efficiency and collection efficiency, and can be directly applied in IceCube analysis. It is different from the usual quantum efficiency measurement, which is based on cathode current response to a calibrated DC light source [16,30].

The laser (Spectra-Physics VSL-337ND-S) emits 4 ns pulses containing $\sim 10^{10}$ photons, as measured by the silicon photodiode probe (Laser Probe, Inc., RjP-465). After a warm-up delay, pulse energies are stable to within $\pm 2\%$.

The beam width is 1 mm, so the illuminated gas volume may be considered as a line source of Rayleigh scattered light. Apertures between the beam and the PMT define a source region with effective length of about 1 cm and a spot size on the PMT of about 1.5 cm. Photons can reach the PMT if they are scattered from the source region into a solid angle of about 7.6×10^{-4} sr around the 90° direction, while other scattered photons are eventually absorbed on baffles or other surfaces inside the chamber.

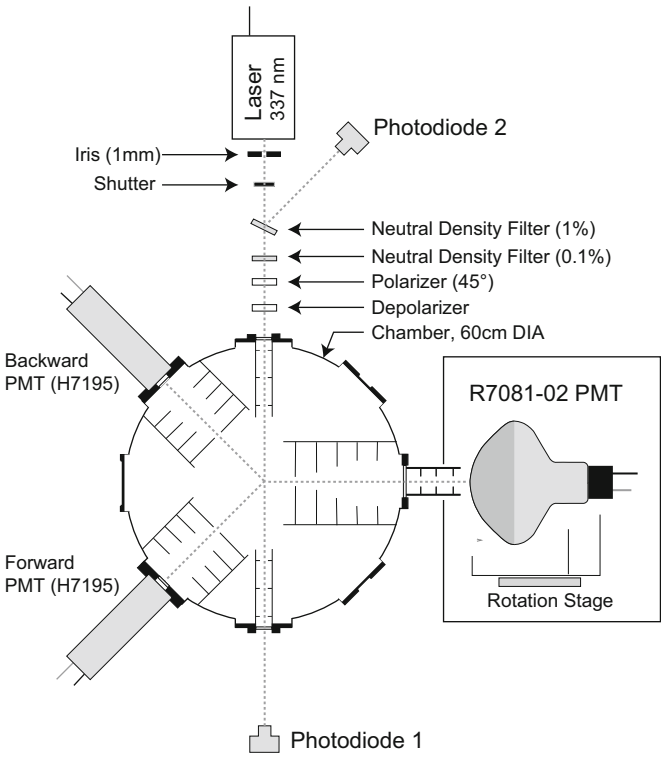

Fig. 8. Schematic view of the absolute calibration system. Photodiode 1 establishes the beam intensity, which is used to predict the amount of Rayleigh-scattered light reaching the R7081-02 PMT. The Hamamatsu H7195 PMTs and the other photodiode are for monitoring. Optical baffles define the scattering geometry, and chamber windows are anti-reflection coated UV quartz ($R<0.1\%$ at 337 nm).

The Rayleigh scattering cross-section for a circularly polarized beam on nitrogen gas is taken as [31]

$$\frac{d\sigma_R}{d\Omega}=\frac{3}{16\pi}(1+\cos^2\theta)\times(3.50\pm 0.02)\times 10^{-26}\,\mathrm{cm}^2 \quad (3)$$

with θ as the polar angle relative to the beam direction. The geometrical integration over the source region and corresponding solid angles is handled in a detailed ray-tracing calculation. After accounting for pressure and temperature, this yields the overall number of scattered photons reaching the PMT, typically 0.5 per pulse. With detection efficiency around 20%, this corresponds to ~ 0.1 SPE per pulse.

For counting photon detections, the PMT output charge is integrated for each laser pulse with a CAMAC ADC. The gating time is 184 ns which is long enough to include the late PMT pulses described in Section 7. The PMT gain is set close to 10^8 as defined by the SPE peak, q_0 in Eq. (1). We then count the number of events with charge q greater than a threshold $q_{\mathrm{th}}=0.5q_0$, which can be clearly discriminated in the charge histogram. A small correction for events with multiple photoelectrons yields the number of detected photons with $q>q_{\mathrm{th}}$.

The PMT efficiency η for $q_{\mathrm{th}}=0.5q_0$ is then given by comparing the number of detected photons to the number reaching the PMT. The efficiency for other charge thresholds can be computed by extrapolation with the SPE charge response model, Eq. (1).

9.2. Results

Fig. 9 shows the measured detection efficiency as a function of distance from the cathode center. It also shows that the absolute

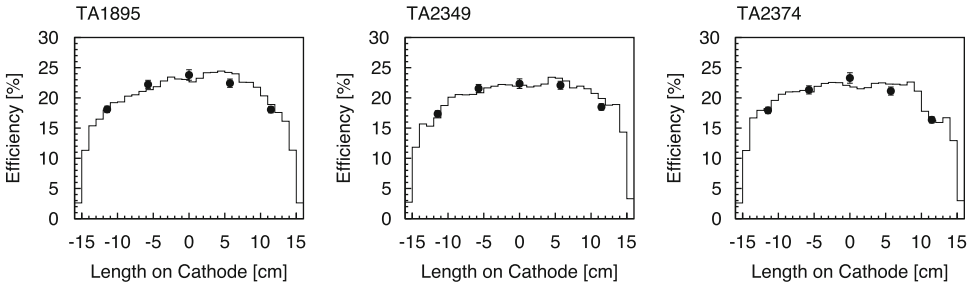

Fig. 9. Detection efficiency as a function of distance from the cathode center for three different PMTs. The points with error bars show absolute efficiency measurements extrapolated to $q_{th}=0$. The histogram curves show corresponding results from the 2D relative efficiency scans (Section 8) after normalization. Systematic uncertainties for the histograms are described in Section 8.

Table 2
Measured photon detection efficiency (η) and photon effective area (A_{eff}) at 25 °C for four different PMTs at wavelength 337 nm and gain 10^8.

PMT	η_{center} (%) ($q_{th}=0.5q_0$)	η_{whole} (%) ($q_{th}=0.5q_0$)	η_{whole} (%) ($q_{th}=0$)	A_{eff} (cm^2) ($q_{th}=0.5q_0$)	A_{eff} (cm^2) ($q_{th}=0$)
TA1895	16.4	13.2	18.6	84	119
TA2086	16.5	13.6	18.8	87	120
TA2349	15.1	12.1	17.6	77	112
TA2374	16.4	13.0	17.8	83	114

Values for $q_{th}=0$ were extrapolated using Eq. (1), where model parameters were fit independently for each PMT.

Table 3
Systematic error budget for the PMT efficiency calibration.

Source	$\Delta\eta/\eta$ (%)
Laser beam energy	5
Aperture	4
Ambient magnetic field	4
Pressure and temperature	1
Polarization	1
Rayleigh cross-section	0.5
Dark noise/cosmic rays	0.2
Overall	7.7

efficiency measurements follow closely the shape expected from the 2D relative efficiency scans (Section 8). Consequently, the relative efficiency scans can be normalized to the absolute measurements and used to estimate the absolute efficiency averaged over any given area of the photocathode surface.

Table 2 lists measured efficiencies at the center and averaged over the whole photocathode area. The latter is defined to include all points within 15 cm of the PMT axis, measured along the curved surface. Table 2 also includes the photon "effective area" which means the amount of ideal surface with 100% efficiency that corresponds to the actual convolution of area and efficiency. Here it is quoted for light uniformly spread over the PMT surface, with normal incidence. For use in IceCube analysis, a similar calculation is performed for unidirectional beams as a function of the beam angle, folding in the variation of cathode response and optical effects at material boundaries.

The detection efficiencies in the central area of the photocathode are close to 20% if extrapolated to $q_{th}=0$. These values have been compared on a PMT-by-PMT basis with measurements by Hamamatsu using cathode response to DC light sources. We find very good agreement, which implies that the collection efficiency is not much less than 100% at the cathode center.

IceCube PMTs operate at lower voltages than used in this measurement (gain 10^7 instead of 10^8), so collection efficiency is expected to be slightly lower. However, this effect is expected to be concentrated at the edges where the electron optics are less ideal, and the efficiency falloff near the edges is obtained from the 2D relative efficiency scans (Section 8). Since those scans were done at gain 10^7, no additional correction is necessary for the results in Table 2.

9.3. Uncertainties

The overall systematic uncertainty $\Delta\eta/\eta$ of the PMT detection efficiency measurement is 7.7%, as detailed in Table 3. In addition, the measurement of each position on the PMT face has a typical statistical uncertainty of about 5%, set by the number of SPE hits recorded. This is reduced to about 2% when calculating efficiency for the whole PMT by combining information from the individual face positions, but the extrapolation relies on the 2D map (Section 8) which has comparable uncertainties.

The dominant contributions to systematic error arise from the laser beam energy measurement, the geometry of the scattering chamber, and the geomagnetic field. The first two enter directly into the calculation of the number of photons reaching the PMT. The beam energy comes from the laser energy probe, which was factory calibrated to within 5% at 337 nm. The aperture uncertainty of 4% comes from geometrical survey of the chamber, which is used in the ray tracing program.

The ambient geomagnetic field is 462 mG and is unshielded in the current setup. By changing the orientation of the PMT, we showed that it affects the point-to-point response map at the 20% level but the average over the surface varies by only 4%.

The Rayleigh scattering angular distribution depends on the polarization of the laser beam [32], so care was required to limit any polarization effect. The effect can be strong because the PMT only sees a Rayleigh scattering signal from the vertical component of polarization: the horizontal component induces a dipole moment oscillating perpendicular to the beam in the horizontal plane, which cannot emit power to the PMT which is in the same direction. On the other hand the energy probe reads the total power regardless of polarization, so the fraction of power in the vertical direction must be under control. In our setup (Fig. 8), the laser beam is first linearly polarized at 45° and then passed through a quartz $\lambda/4$ waveplate to convert it to 100% circular polarization. By rotating a linear polarizer in the beam, we verified that the resulting horizontal and vertical components are equal to within better than 1%, which leads to a limit of 1% for the corresponding systematic effect on the efficiency measurement.

Several analyses were performed to show that the scattered photons are coming from Rayleigh scattering and not other sources such as residual suspended dust. We checked for expected scaling with gas density down to low pressure, symmetry of scattered light seen in forward and backward

monitoring PMTs (see Fig. 8), and repeatability of measurements after long time intervals.

The main systematic uncertainties in our method could be reduced if desired, comparable to the current statistical precision of about 2%. To accomplish this, one would calibrate the silicon photodiode "energy meter" at the 1% level; measure the aperture geometry more precisely; and provide good shielding from the geomagnetic field.

9.4. Additional corrections

There are additional steps to obtain the detection efficiency of DOMs from the PMT efficiency measurements, and these will be reported separately along with other studies on assembled DOMs. Corrections include attenuation of light in the glass pressure housing and the gel used for optical and mechanical coupling, wavelength dependence in both the PMT sensitivity (quoted by the manufacturer [16]) and the attenuation factors, and the geometry of incident rays. These effects are included in a detailed optical simulation of the DOMs [27,33] which will be compared to laboratory measurements on assembled DOMs. A full detector simulation can be used to combine the absolute efficiencies at 337 nm, the wavelength dependences, and the spectrum of light received from neutrino interactions. Investigations of the combined effect show that IceCube detects signal photons in a broad range centered on about 400 nm. These studies will be presented elsewhere.

Our measurements were at 25 °C, and some temperature dependence can be expected. The manufacturer quotes a temperature coefficient of −0.2%/°C for cathode sensitivity [16]. This is being directly addressed by relative measurements of optical efficiency of assembled DOMs at −45, −20 °C and room temperature.

10. PMT linearity and saturation behavior

For most neutrino interactions expected in IceCube, any one PMT will not detect more than a handful of photons. For such events, and even when up to a few hundred are detected, the PMT output is proportional to the number of photons detected. However, some of the most interesting signal events would be expected to deposit large amounts of energy within tens of meters of individual PMTs, and then the PMT response can be less than proportional. Optimal reconstruction requires measuring the linearity limit and modeling the nonlinear saturation behavior.

To study saturation behavior, PMTs were illuminated with LED pulses of various durations and brightnesses. The duration of the light pulses was varied from 3 ns to 1 μs, as measured with a fast PIN photodiode (1 ns response time). A set of calibrated neutral density filters was used to control the light level. For a given LED brightness, illumination was first measured by the PMT signal, using a filter with sufficient attenuation to allow linear operation of the PMT. The observed signal was converted to a photoelectron rate and a total number of photoelectrons (p.e.) using the SPE charge q_0, determined in a separate step. Then the illumination level was increased by using different filters, with the new number of p.e. calculated from the ratio of filter attenuation coefficients.

Fig. 10(a) shows the observed peak anode current I as a function of the ideal peak current I_0, defined as the peak p.e. rate times the SPE charge. At gain 10^7, the PMT response is linear within 10% up to currents of about 50 mA (31 p.e./ns), but saturates completely at about 150 mA. Peak responses to different light pulse widths from 3 to 400 ns lie along a single curve. The 3 and 20 ns width pulses were approximately Gaussian in shape, so the observation of identical peak response supports a saturation model where the observed current is a direct function

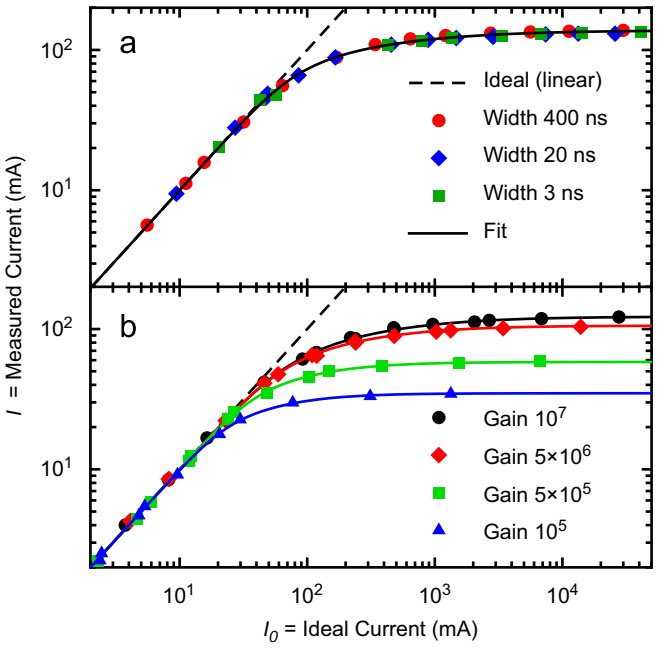

Fig. 10. (a) PMT saturation curve for gain 10^7. The measured current is plotted against the instantaneous light level, defined in terms of the current that would be expected for an ideal (linear) device. Data points correspond to peak currents for the indicated pulse widths. The fit curve is given by Eq. (4), with parameters chosen optimally for this PMT (serial number SA2747). (b) Effect of PMT gain on the saturation curve. Data points correspond to peak currents for 200 ns pulses for PMT serial number AA0020. The curves show the fitted parameterization, Eq. (5).

of the instantaneous illumination, with little cumulative effect from previous illumination. In particular the data are inconsistent with models expressed in terms of total pulse charge, which were used in some older versions of the IceCube simulation software. The 400 ns pulses were approximately rectangular in shape and the output current mirrored this shape well even in the saturation region, again as expected for an instantaneous current saturation model. Even long light pulses near saturation level show only about 5% decline from 100 mA after 1 μs of steady illumination. (Note this small history effect is independent of the transient gain loss due to discharge of the dynode capacitors, which remains below 1% for such a pulse.)

The same saturation behavior was found to apply regardless of what part of the cathode was illuminated, even at −30 °C, which indicates that photocathode surface resistance [16] is not important on the relevant time scales.

The instantaneous current response is well parameterized by the following:

$$\ln I_0 = \ln I + C\frac{(I/A)^B}{(1-I/A)^{1/4}}. \tag{4}$$

The parameters A, B and C differ substantially from one PMT to another (Table 4), so the model should not be used to invert observed saturated pulses unless each PMT is fully characterized.

Fig. 10(b) shows additional measurements at a range of lower gains down to 10^5, relevant for IceTop DOMs. The model of Eq. (4) continues to apply over the full range if the parameters are scaled approximately as powers of the gain, as shown by the curves which are scaled by $\gamma \equiv \text{Gain}/10^6$:

$$A(\gamma) = 285\gamma^{0.52}/(1+\gamma^{1/4})^2$$

$$B(\gamma) = 13\gamma^{0.18}/(1+\gamma^{1/4})^2$$

$$C(\gamma) = 0.32\gamma^{-0.13}(1+\gamma^{1/4})^2. \tag{5}$$

The given parameters apply to a single measured PMT, but similar scaling behavior can be expected for other examples; as a first estimate one would adjust the leading coefficients in each parameter to match measurements at a particular gain, and retain the same scaling with gain. Note the good numerical behavior of the scaling equations allows them to be used also for estimates outside the given range of gain.

The instantaneous current model also helps understand how the response to narrow light pulses (3 ns FWHM) broadens as intensity increases (Fig. 11). With the light pulse strongly attenuated (220 p.e.), the PMT output pulse width is similar to the SPE response, about 10 ns. As more light is allowed to reach the PMT (3700 p.e.), first a gradual broadening occurs to about 20 ns width. This broadening follows from Eq. (4) because the peak current is more attenuated than the rising and trailing edges. At this point a tail is visible, along with a second peak delayed by about 60 ns relative to the main peak. These are consistent with the late photoelectron responses seen in SPE time resolution measurements (Section 7), except that the relative sizes of main peak and tail are altered by saturation in the main peak. At still higher light levels (210,000 p.e.), the second tail peak is comparable in size to the fully saturated main peak, and the total width is dominated by the combination of the two peaks.

The highest light level in Fig. 11 also exposes a small pre-pulse 30 ns before the main peak, as well as a substantial afterpulse starting several hundred ns later (see Section 11). The pre-pulse is ascribed to photoelectrons ejected from the first dynode, and is somewhat exaggerated in Fig. 11 because the light source was aimed at the center of the cathode with the dynode directly behind. The individual quanta comprising the pre-pulse were separately studied using SPE-level illumination, and were found to be between 1/10 and 1/20 of the SPE pulse size, occurring at less than 1% of the SPE rate. The ratio between sizes of SPE pulses and pre-pulse quanta is similar to the typical first dynode gain reported by the manufacturer [24]. Because individual pre-pulse quanta are below threshold for triggering DOMs, they have a small impact on event reconstruction. The combined pre-pulses from many photons would only be observable for a large, narrow light pulse ($\sim$5000 photons detected within 30 ns). Pulses originating more than $\sim$25 m from a DOM would generally be broader than this, due to scattering in the ice [7].

The saturation model (Eq. (4)) can be important for reconstruction of very high energy neutrinos that produce electromagnetic or hadronic showers. Ideally, reconstruction would rely most heavily on the PMTs closest to a shower, because the light pulse is broadened and attenuated as it travels through the ice [7]; however, these PMTs can be saturated for high energy events. The energy where saturation effects become important can be estimated by choosing a characteristic distance of 60 m, which is about half the inter-string spacing. At this distance, simulations [20] show that a 600 TeV shower yields peak intensity of 30 p.e./ns, equivalent to the linearity limit of 50 mA. Above this energy, signals in close PMTs require a correction for saturation. Above $\sim$10 PeV, many nearby PMTs are badly saturated and the shower energy measurement must rely mostly on far-away PMTs. However, even badly saturated PMTs measure the beginning and end of the pulse, which can be used to constrain the event geometry.

Table 4
Saturation curve parameters for three PMT samples, as defined for Eq. (4).

PMT serial no.	A (mA)	B	C
AA0020	126	2.02	2.98
SA2747	138	2.05	3.23
SA2749	138	1.82	2.67

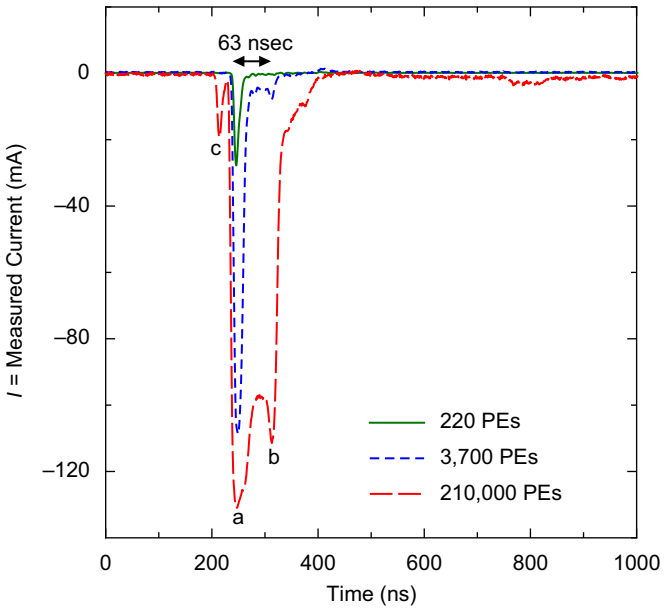

Fig. 11. Average waveforms observed in PMT serial number SA2747 for 3 ns (FWHM) light pulses with progressively higher intensity: (a) main peak; (b) secondary peak due to unusual electron trajectories and (c) pre-pulse.

11. Afterpulses

As shown in Figs. 6 and 11, the prompt response to a light pulse has a tail extending to about 100 ns. Afterpulses are seen in the range of 300 ns to 11 μs. Such afterpulses are a common feature of PMTs, and are attributed to ionization of residual gases by electrons accelerated in the space between dynodes [34]. Ions created in this way can be accelerated back to the photocathode, causing ejection of electrons which are subsequently amplified like the original photoelectrons. Some ions strike one of the dynodes instead, but the corresponding ejecta are amplified much less and could easily go undetected.

Afterpulse measurements were made at 25 °C with LED pulses of 40 ns width, using calibrated optical attenuators to control the intensity, as for the saturation measurements (Section 10). In a bright LED flash, many individual ions are created, and their responses add up to an afterpulse waveform with well defined peaks and valleys (Fig. 12). The various peaks are believed to correspond to ions of different masses, according to their individual flight times in the accelerating field [34]. Prominent afterpulse peaks for this PMT occur around 600 ns, 2 and 8 μs after the main response peak. The peaks are fairly wide and no period is entirely devoid of afterpulses until after 11 μs.

The average afterpulse waveform grows almost linearly with the flash brightness even up to the highest intensity studied (4.4×10^6 p.e. in 40 ns), where the primary response is completely saturated at $\sim$1000 p.e./ns (Fig. 10). This suggests that observed afterpulses arise primarily from ions generated in earlier stages of the multiplier, whose electron currents continue to rise even when later stages have saturated.

Up to primary pulses of 1×10^6 p.e., the integral from 300 ns to 11 μs corresponds to 0.06 SPE per primary photoelectron.

For dimmer flashes, individual events have a small number of afterpulse electrons. These appear as separate single afterpulses distributed in time, with probability that can be approximately

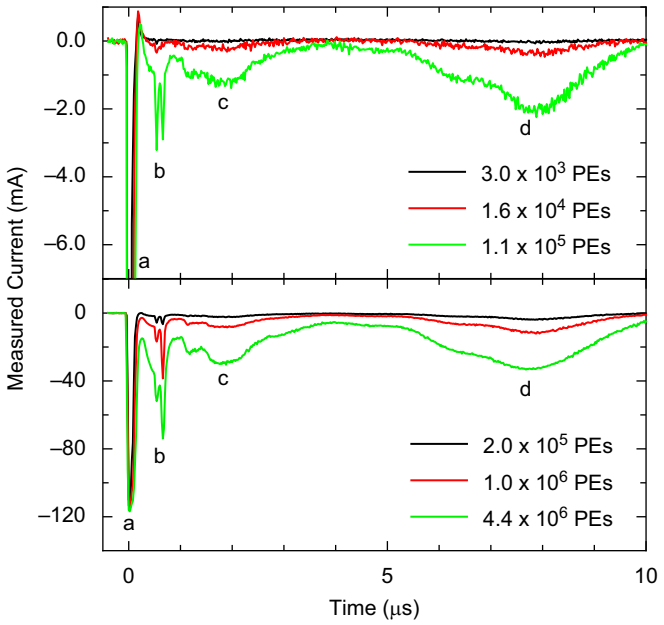

Fig. 12. PMT afterpulse waveforms for bright flashes lasting 40 ns. Each curve is averaged over many flashes. The primary response (a) is off-scale and saturated at most of these intensities. Brightness of flashes is determined by the method of Section 10, which is independent of PMT saturation effects. Prominent afterpulse peaks are seen around (b) 600 ns, (c) 2 μs and (d) 8 μs after the primary response. The afterpulse waveforms grow nearly linearly with flash intensity up to the maximum intensity measured. The PMT was operated at gain of 10^7, with the anode at 1326 V. Some variation in afterpulse waveforms is observed from one PMT to another of the same type. Measurement of tails at very late times is slightly affected by an AC coupling time constant of 80 μs.

predicted from the average waveforms of Fig. 12. Because different ions are associated with different time ranges, and because some ions eject multiple electrons from the photocathode, each afterpulse delay range will be characterized by a different fundamental charge distribution. We have observed corresponding peak charges from 1 SPE to 13 SPE, consistent with a recent more detailed study of individual ion afterpulses [35].

The above observations are from study of only a few PMT samples, and the numbers quoted pertain to only one (serial AA0020). Although quantitative differences are seen from one sample to another, the information allows one to assess whether afterpulses affect IceCube event reconstructions, and to limit small systematic errors. If a particular physics analysis then appears sensitive to afterpulses, a larger sample of PMTs would have to be studied quantitatively to provide the necessary corrections.

Given the small ratio of charge between afterpulse and primary pulse, it can be expected that most IceCube analyses will not be strongly sensitive to the details of afterpulses. Typical IceCube events yield hits in each PMT that are spread over times of a few hundred nanoseconds, well before the main part of the afterpulse distribution. For very high energy events (e.g. electron energy 1 PeV in the deep ice), signals are likely to be seen by PMTs 500 m away where arrival times are dispersed over 2 μs (FWHM), and then the afterpulse distribution becomes more relevant. However, the main effect is a minor distortion of the late part of the pulse, which already has an intrinsically long tail due to scattering. Generally one does not lose much information by disregarding details of the waveforms at late times.

However, some events can have multiple peaks in the photon time distributions, and then a characterization of afterpulses can be important for proper reconstruction. The most common case is an event with coincident arrival of one or more downgoing muons from cosmic ray showers above the detector, which calls for disentangling the hits originating from multiple tracks, and therefore also the afterpulses. Multiple muons can also arise from a single shower, and when the resulting tracks are well separated they can yield multiple hits. More intriguing is the possibility of ν_τ interactions which can create two showers of particles separated by hundreds of meters [36]. In such a case some PMTs can see pulses of light separated by a few microseconds, so effects of afterpulses should be considered carefully. The late pulses described in Section 7 should also be considered in these contexts.

12. Summary

The R7081-02 PMT has been characterized and key findings were discussed in the context of IceCube physics goals. We observe a single-photoelectron time resolution of 2.0 ns averaged over the face of the PMT. A small fraction of the pulses arrive much later, with about 4% between 25 and 65 ns late. We also observe prepulsing and afterpulsing, with afterpulsing occurring up to 11 μs late. The single photoelectron charge spectrum is well fit by a Gaussian corresponding to charge resolution near 30%, plus a contribution at low charge which is represented by an exponential. The dark rate was measured to be 300 Hz in the temperature range −40 to −20 °C. A new method for optical sensitivity calibration has been demonstrated, which uses Rayleigh scattering to scale from the intensity of a primary laser beam to the much smaller number of photons reaching a target PMT. Measurements of dark rate, single photon detection efficiency, single photoelectron waveform and charge, time resolution, large pulse response, and afterpulses will serve as input for detailed simulation of IceCube physics events.

Acknowledgements

We acknowledge support from the following agencies: U.S. National Science Foundation-Office of Polar Program, U.S. National Science Foundation-Physics Division, University of Wisconsin Alumni Research Foundation, U.S. Department of Energy, and National Energy Research Scientific Computing Center, the Louisiana Optical Network Initiative (LONI) grid computing resources; Swedish Research Council, Swedish Polar Research Secretariat, and Knut and Alice Wallenberg Foundation, Sweden; German Ministry for Education and Research (BMBF), Deutsche Forschungsgemeinschaft (DFG), Research Department of Plasmas with Complex Interactions (Bochum), Germany; Fund for Scientific Research (FNRS-FWO), FWO Odysseus programme, Flanders Institute to encourage scientific and technological research in industry (IWT), Belgian Federal Science Policy Office (Belspo); Marsden Fund, New Zealand; Japan Society for the Promotion of Science (JSPS); M. Ribordy acknowledges the support of the SNF (Switzerland); A. Kappes and A. Groß acknowledge support by the EU Marie Curie OIF Program; J.P. Rodrigues acknowledge support by the Capes Foundation, Ministry of Education of Brazil.

References

[1] J. Ahrens, et al.IceCube Collaboration, Astropart. Phys. 20 (2004) 507.
[2] J. Ahrens, et al., IceCube Collaboration, IceCube Preliminary Design Document, 2001 〈http://icecube.wisc.edu/〉.
[3] T.K. Gaisser, F. Halzen, T. Stanev, Phys. Rep. 258 (1995) 173;
J.G. Learned, K. Mannheim, Annu. Rev. Nucl. Part. Sci. 50 (2000) 679;
F. Halzen, D. Hooper, Rep. Prog. Phys. 65 (2002) 1025.
[4] A. Karle for the IceCube Collaboration, IceCube, in: Proceedings of the 31st International Cosmic Ray Conference, 7–15 July 2009, Lodz, Poland.

[5] W. Lohmann, R. Kopp, R. Voss, Energy loss of muons in the energy range 1–10 000 GeV, CERN Report 85–03, 1985.
[6] D. Chirkin, W. Rhode, preprint arXiv:hep-ph/0407075v2, 2008.
[7] M. Ackermann, et al., J. Geophys. Res. 11 (2006) D13203.
[8] D. Chirkin for the IceCube Collaboration, in: Proceedings of the 30th International Cosmic Ray Conference, 3–11 July 2007, Merida, Yucatan, Mexico, session HE1.5; in arXiv:0711.0353 [astro-ph], pp. 151–154.
[9] E. Andres, et al.AMANDA Collaboration, Astropart. Phys. 13 (2000) 1.
[10] J. Ahrens, et al.AMANDA Collaboration, Phys. Rev. D 66 (2002) 12005.
[11] E. Middell, J. McCartin M. D'Agostino for the IceCube Collaboration, in: Proceedings of the 31st International Cosmic Ray Conference, 7–15 July 2009, Lodz, Poland.
[12] T. Gaiser et al., IceCube Collaboration, IceTop Preliminary Design Document, 2003 〈http://icecube.wisc.edu/〉.
[13] A. Achterberg, et al.IceCube Collaboration, Astropart. Phys. 26 (2006) 155.
[14] R. Abbasi, et al.IceCube Collaboration, Nucl. Instr. and Meth. A 601 (2009) 294.
[15] Hamamatsu Corp., R7081-02 Photomultiplier Tube Data, 2003.
[16] Hamamatsu Corp., Photomultiplier Tubes: Basics and Applications, third ed., 2007.
[17] A. Ankowski, et al., Nucl. Instr. and Meth. A 556 (2006) 146;
J.A. Nikkel, W.H. Lippincott, D.N. McKinsey, J. Instrum. 2 (2007) 1004;
H.O. Meyer, preprint arXiv:0805:0771v1 [nucl-ex], 2008.
[18] A.S. Dighe, M.Th. Keil, G.G. Raffelt, J. Cosmol. Astropart. Phys. 0306 (2003) 005.
[19] EMCO High Voltage Corporation, Sutter Creek, CA.
[20] J. Lundberg, et al., Nucl. Instr. and Meth. A 581 (2007) 619.
[21] R. Dossi, et al., Nucl. Instr. and Meth. A 451 (2000) 623.
[22] P.B. Coates, J. Phys. D Appl. Phys. 6 (1973) 153.
[23] O.Ju. Smirnov, P. Lombardi, G. Ranucci, Instrum. Exp. Tech. 47 (2004) 69.
[24] Hamamatsu Corp., Personal communication.
[25] B.K. Lubsandorzhiev, P.G. Pokhil, R.V. Vasiljev, A.G. Wright, Nucl. Instr. and Meth. A 442 (2000) 452.
[26] A. Karle, Monte Carlo simulation of photon transport and detection in deep ice: muons and cascades, in: Proceedings of the Workshop on Simulation and Analysis Methods for Large Neutrino Telescopes, DESY 1998.
[27] K. Hoshina 〈http://www.ppl.phys.chiba-u.jp/ROMEO/〉.
[28] D. Motta, S. Schönert, Nucl. Instr. and Meth. A 539 (2005) 217.
[29] S. Fukuda, et al.The Super-Kamiokande Collaboration, Nucl. Instr. and Meth. A 501 (2003) 418;
A. Aguilar, et al., Astropart. Phys. 23 (2005) 131.
[30] R. Mirzoyan, et al., Nucl. Instr. and Meth. A 572 (2007) 449.
[31] H. Naus, W. Ubachs, Opt. Lett. 25 (2000) 347 and references therein..
[32] W. Reckers, Y. Gu, E.W. Rothe, H. Voges, Appl. Spectrosc. 51 (1997) 1012.
[33] S. Agostinelli, et al., Nucl. Instr. and Meth. A 506 (2003) 250.
[34] P.B. Coates, J. Phys. D 6 (1973) 1159.
[35] K. J. Ma, et al., preprint arXiv:0911.5336v1 [physics.ins-det], 2009.
[36] J.G. Learned, S. Pakvasa, Astropart. Phys. 3 (1995) 267.